The breaking of interfacial waves at a submerged bathymetric ridge

ERIN L. HULT[1]†, CARY D. TROY[2]
AND JEFFREY R. KOSEFF[1]

[1]Department of Civil and Environmental Engineering, Stanford University, Stanford, CA 94305, USA

[2]Department of Civil and Environmental Engineering, Purdue University, West Lafayette, IN 47907, USA

The breaking of periodic progressive two-layer interfacial waves at a Gaussian ridge is investigated through laboratory experiments. Length scales of the incident wave and topography are used to parameterize when and how breaking occurs. Qualitative observations suggest both shear and convection play a role in the instability of waves breaking at the ridge. Simultaneous particle image velocimetry (PIV) and planar laser-induced fluorescence (PLIF) measurements are used to calculate high resolution, two-dimensional velocity and density fields from which the local gradient Richardson number Ri_g is calculated. The transition to breaking occurred when $0.2 \leqslant Ri_g \leqslant 0.4$. In these wave-ridge breaking events, the destabilizing effects of waves steepening in shallow layers may be responsible for breaking at higher Ri_g than for similar waves breaking through shear instability in deep water (Troy & Koseff, *J. Fluid Mech.*, vol. 543, 2005*b*, p. 107). Due to the effects of unsteadiness, nonlinear shoaling and flow separation, the canonical $Ri_g > 0.25$ is not sufficient to predict the stability of interfacial waves. A simple model is developed to estimate Ri_g in waves between finite depth layers using scales of the incident wave scale and topography. The observed breaking transition corresponds with a constant estimated value of Ri_g from the model, suggesting that interfacial shear plays an important role in initial wave instability. For wave amplitudes above the initial breaking transition, convective breaking events are also observed.

1. Introduction

Internal wave breaking is thought to be a major cause of vertical mixing in the ocean. Despite the importance of this process, breaking events are very difficult to observe in the field and the physical processes leading to the mixing are not completely understood. The question of whether shear or convective instability leads to the breaking of oceanic internal waves has led to substantial debate. The nature of the instability is important, not simply as an academic exercise, but because the mixing efficiency can vary significantly depending on the type of instability. The accuracy of this internal wave breaking efficiency is crucial for parameterizing these processes in global ocean models. The mixing efficiency of a purely convective instability has been shown to be 0.5 (Linden & Redondo 1991) whereas the efficiency of shear instability measured in a range of laboratory experiments and numerical simulations tends to

† Email address for correspondence: ehult@stanford.edu

be about 0.2 (Peltier & Caulfield 2003). Although a constant efficiency for internal wave breaking is often assumed for model parameterization, breaking mechanisms can vary significantly under different conditions. This paper examines when and how periodic interfacial waves break when they interact with a ridge. Elevated turbulent diffusivities have been observed over rough bathymetry, suggesting that substantial diapycnal mixing may occur at submerged ridges and sea mounts due to internal wave breaking (Lueck & Mudge 1997; Polzin *et al.* 1997; Toole *et al.* 1997; Ledwell *et al.* 2000). The two main goals of the paper are (i) to use incident wave and topographic scales to classify when and how interfacial waves break at a ridge, and (ii) to investigate whether the local gradient Richardson number is a good predictor of breaking in these wave events. These goals are investigated through laboratory experiments, using the spatially and temporally resolved methods of planar laser induced fluorescence (PLIF) and particle image velocimetry (PIV).

The layout of this paper is as follows. In §2, background information on the breaking of internal waves at bathymetry is provided. The methods and facility are described in §3. In §4, the results on wave breaking are presented and in §5 these results are discussed and compared with a simple theoretical model. Conclusions are presented in §6.

2. Background

2.1. *Breaking internal waves*

Two main processes are proposed for the initiation of instability of interfacial waves: shear instability at the interface and gravitational or convective instability due to wave steepening. In the study of the stability of interfacial waves, the stability criterion for stratified parallel shear flows is often applied. The stability of stratified parallel inviscid shear flows is governed by the Taylor–Goldstein equation, which can be solved to provide a gradient Richardson number criterion for stability, where

$$Ri_g \equiv \frac{N^2}{\frac{\partial u}{\partial z}^2}, \qquad (2.1)$$

and $N^2 = (-g/\rho_0)(\partial \rho/\partial z)$. Linear stability is guaranteed for perturbations of all wavelengths if $Ri_g > 1/4$ everywhere in the flow. If $Ri_g < 1/4$ at any location, the flow may or may not be unstable (Howard 1961; Miles 1961). Phillips (1966) proposes that high shear at the crests and troughs of interfacial waves can lead to interfacial instability. Orlanski & Bryan (1969) argue that overturning driven by gravitational instability will always occur when the local fluid velocity u exceeds the phase speed of the wave c_p; hence the local $Fr > 1$ and suggest that in a linear stratification, instability due to shear should require four times the energy required for convective instability, and thus convective instability is likely to dominate internal wave breaking.

Recent work (Troy & Koseff 2005*b*; Fructus *et al.* 2009), however, has pointed out the shortcomings of the application of steady, uniform instability criteria to breaking internal waves; the extreme unsteadiness and non-uniformity of the flow field renders the gradient Richardson number and Froude number (u/c_p) insufficient predictors of instability.

Recent field observations show dramatic qualitative evidence of shear instability in the breaking of internal solitary waves of depression over the continental shelf (Moum *et al.* 2003). Grue *et al.* (2000) observe structures suggestive of shear instability but suggest that, generally, waves observed tend to break when $u/c_p > 1$. De Silva

et al. (1996) compare the development of Kelvin–Helmholtz billows observed in the lab with field observations of turbulence in internal solitary waves and find similar billow growth rates, suggesting overturning observed in the field may be due to shear instability. For periodic long interfacial waves, Troy & Koseff (2005*b*) observe breaking due to shear instability at the crests and troughs of progressive waves in the laboratory. In numerical simulations, Fringer & Street (2003) observe shear instability leading to convective instability and weak convective instability for intermediate and shorter waves, respectively. The breaking of internal waves along topographic slopes has also been investigated (Thorpe 1987; Ivey & Nokes 1989; Taylor 1993).

2.2. *Breaking at topography*

A number of studies have examined the process of internal waves shoaling and breaking on bathymetric features such as slopes, shelves and ridges. When first mode periodic waves in a continuous stratification interact with a slope, intense mixing occurs near the bed for waves of critical slope (Cacchione & Wunsch 1974; Ivey & Nokes 1989; Ivey, Winters & De Silva 2000). Field observations of shoaling internal waves have captured a range of breaking events, including dense water boluses advected up-slope (Emery & Gunnerson 1973). Similar boluses were observed in laboratory experiments after gravitational instability developed in two-layer progressive wavetrain interactions with a shoaling shelf (Wallace & Wilkinson 1988) and in the numerical simulations of first mode waves in a continuous stratification (Venayagamoorthy & Fringer 2006).

Laboratory and numerical studies on internal wave interactions with topography suggest that breaking through shear instability may occur, but as the nonlinearity of the event is increased, more vigorous mixed or convective breaking dominates. In laboratory experiments, internal solitary waves of depression shoaling on a uniform slope became unstable through shear instability on the rear face of the wave (Kao, Pan & Renouard 1985) and through mixed or convective overturning in more intense interactions (Helfrich & Melville 1986). Strong, down slope flow from previous breaking waves can intensify the breaking of incident shoaling waves (Helfrich & Melville 1986; Wallace & Wilkinson 1988; Sveen *et al.* 2002; Vlasenko & Hutter 2002). Sveen *et al.* (2002) observed convective breaking in lab experiments on internal solitary wave interactions with a ridge, with shear instability also observed during the strongest wave-ridge interactions. Shear instability, preceding convective instability, during very strong wave-slope interactions was observed by Boegman, Ivey & Imberger (2005).

While many studies have looked at wave interactions with a slope or shelf, limited work has looked at the case of interfacial waves breaking at a ridge (Wessels & Hutter 1996; Sveen *et al.* 2002; Chen *et al.* 2008). The dynamics of wave breaking at a ridge can be somewhat different than the slope and shelf cases. When the interface intersects the slope of the ridge, wave breaking would likely be very similar to the slope case. When the ridge crest is below the density interface, however, wave breaking is no longer focused along the slope and additional parameters, such as the height of the interface over the ridge, may impact wave breaking. In the ridge case, waves tend to shoal as they approach the ridge, and then become less steep as they pass beyond the ridge, complicating the breaking dynamics. The present study investigates wave interactions with similar bathymetry to Sveen *et al.* (2002), but focuses on periodic progressive wave trains rather than solitary waves.

2.3. *Breaking criteria*

A variety of breaking criteria have been developed for predicting when interfacial waves will break. A theoretical estimate for the critical wave steepness, ka, for wave

instability can be determined for interfacial waves with a finite interfacial thickness (Thorpe 1978) and for an infinitely thin interface (Holyer 1979). Both the wave steepness ka and u/c_p are measures of wave nonlinearity and are sometimes used to assess whether convective instability will develop in surface and interfacial waves. The minimum value of Ri_g and the maximum value of u/c_p are commonly used as indicators of instability, but these metrics must be known over the spatial and temporal extent of the event. Because these dynamic metrics may be very costly to measure, the ideal predictive breaking criteria would be based on incident wave and topographic length scales.

Many studies have used scales of the wave and topography to describe when interfacial wave breaking occurs, often following the parameterization of surface wave breaking. These parameterizations aim to provide some predictive capability for wave breaking and are typically based on quantities such as length scales that are easier to measure than $Ri_g(x, y, z, t)$ or $u(x, y, z, t)/c_p$. Shoaling surface waves become unstable when the amplitude scaled by the local depth reaches the constant value of $a/h = 0.39$, with this ratio increasing significantly when the beach slope is greater than $1/40$ (e.g. Dean & Dalrymple 1984). For a slope-shelf geometry, Helfrich & Melville (1986) apply a similar criterion for interfacial waves and show that solitary waves propagate up-slope without instability when $a_0/h_1 \lesssim 0.3$, where a_0 is the amplitude of the solitary wave and h_1 is the local depth of the lower layer. Weak interfacial shear instabilities occurred for $0.3 < a/h_1 < 0.4$, with strong convective overturning when $a/h_1 \gtrsim 0.4$. For solitary waves shoaling on a uniform slope without a shelf present, similar results are obtained, with breaking occurring for $a/h_1 \gtrsim 0.3$ (Helfrich 1992). Vlasenko and Hutter (2002) suggest a bed slope-dependent breaking criterion for solitary waves on slope-shelf bathymetry where $a/h_1 = 0.8°/\gamma + 0.4$, where γ is the angle of the slope from the horizontal direction, based on quasi-two-layer numerical simulations. Wave slope and bed slope have been shown to affect internal solitary wave breaking on a slope as well (Nagashima 1971; Michallet & Ivey 1999), and an internal Irribarren number comparing the wave steepness and the bed slope has been used to distinguish the regimes when spilling, plunging and collapsing breaking of solitary waves occur (Boegman *et al.* 2005).

While the parallel steady inviscid shear flow stability criterion of $Ri_g \geqslant 0.25$ has often been applied to internal wave flows, there is some question as to whether the assumptions of parallel steady shear flow are valid. Furthermore, although $Ri_g \leqslant 0.25$ is a necessary but insufficient condition for shear instability in a steady parallel inviscid flow, a wide range of ocean models assume turbulence occurs wherever Ri_g falls below 0.25. The validity of the steady and uniform assumptions depend on how the unsteadiness time scale λ/c_p compares with the time scale of instability growth and how the wavelength, λ compares with the spatial scale of the instability (e.g. Kao *et al.* 1985; Troy & Koseff 2005*b*). In a recent review paper, Helfrich & Melville (2006) state that neither field observations nor lab experiments that have suggested that interfacial waves may break through shear instability have had sufficient resolution to determine the local Richardson number. To verify whether the shear stability criterion is appropriate, the spatial and temporal resolution of density and velocity measurements must be sufficient to capture the local minimum in Ri_g.

Several methods have been used to measure Ri_g directly. Kao *et al.* (1985) estimated Ri_g in a shoaling solitary wave by measuring the displacement of a column of hydrogen bubbles to estimate the shear profile and found the minimum Ri_g to be near or below 0.25 for unstable cases, which was consistent with their KdV model results. Fructus *et al.* (2009) measured the velocity in internal solitary waves and
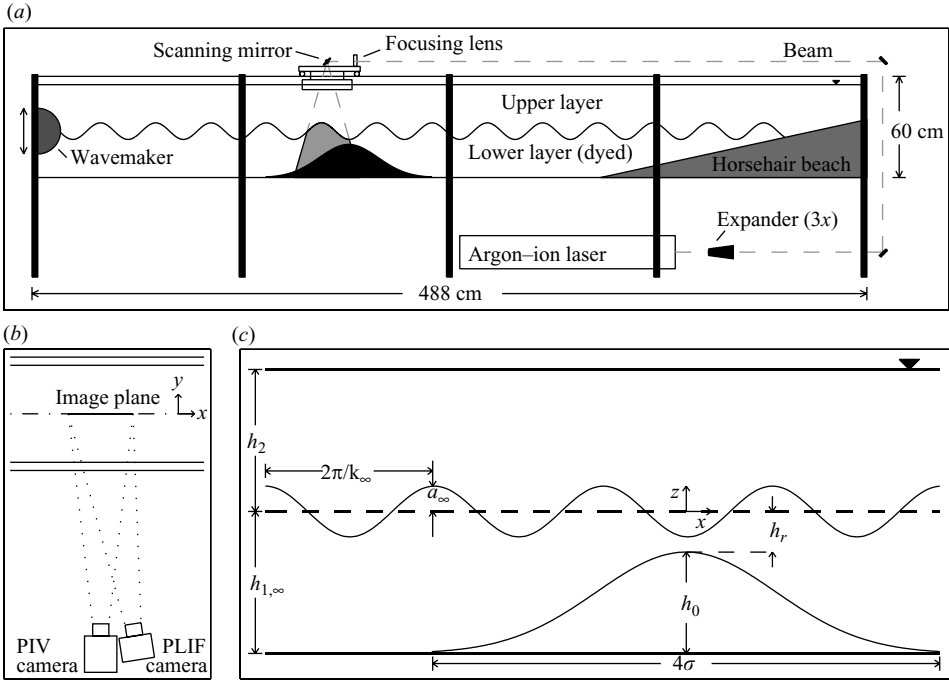
FIGURE 1. (*a*) A schematic of the tank and PIV/PLIF imaging system. (*b*) An aerial view of camera set-up for simultaneous PIV/PLIF imaging. (*c*) Key wave and topography parameters.

paired that with a theoretical density field for the observed wave parameters so that Ri_g could be calculated. While this is an elegant solution for idealized conditions, the theoretical density field cannot be calculated for the complex bathymetric interaction in the wave-ridge case. Dalziel *et al.* (2007) have developed a system to obtain two-dimensional simultaneous density and velocity measurements using synthetic schlieren and PIV, stressing the need for simultaneous measurements in order to capture key dynamics in nonlinear stratified flows. A sample calculation of $Ri_g(x, z)$ in a solitary wave was presented by Dalziel *et al.* (2007). Combined PIV/PLIF has been used by Pawlak & Armi (2000) and Zhu & Lawrence (2001) to measure the local gradient Richardson number in two-layer shear flows. In this paper, we use combined PIV/PLIF to obtain high-resolution measurements of the wave field.

2.4. *Non-dimensionalization*

The wave-ridge interaction of this study is controlled by 11 dimensional parameters: layer depths h_1 and h_2, the height of the ridge h_0, the standard deviation of the Gaussian ridge σ, the height of the interface above the ridge h_r, the wave amplitude a, the wavenumber k, the interfacial thickness δ, the viscosity ν, the diffusivity of the stratifying scalar κ and the reduced gravity $g' = 2g(\rho_1 - \rho_2)/(\rho_1 + \rho_2))$, where the length scales are shown in figure 1(*c*). From these 11 parameters, 9 dimensionless groups can be formed, including a Reynolds number $Re = a^2(g'/\delta)^{1/2}/\nu$, a Schmidt number $Sc = \nu/\kappa$ and 7 length scale ratios: the wave steepness ka, scaled wavenumbers $k\delta$ and $k\sigma$, scaled layer depths kh_1 and kh_2, ridge slope $h_0/2\sigma$ and a scaled amplitude a/h_r.

In this study, the most important parameters are thought to be the scaled amplitude a/h_r, the scaled wavelength $k\delta$ and the wave steepness ka. These three parameters as

well as a Richardson number which can be estimated from the other dimensionless parameters (see §5.1) are used to study the role of shear and nonlinearity in wave breaking at the ridge. The ridge slope may affect breaking behaviour (e.g. Vlasenko & Hutter 2002), but this parameter is not varied in this study. Here, $h_0/2\sigma = 0.4$, which is comparable to bathymetric slopes of 0.07–0.5 where enhanced diapycnal diffusivities have been observed (Kunze & Sanford 1996; Toole *et al.* 1997). The parameter $k\sigma$ is varied, but this parameter is not thought to have a major impact on the flow except perhaps in the knife-edge limit, when the flow is very long relative to the ridge ($k\sigma < 1$). Low values of $h_0/2\sigma$ and $k\sigma$ are limited by the length of the laboratory facility. The Reynolds number may impact when separation over the ridge occurs (see §4.4). The Schmidt number is held constant.

3. Experimental methods

3.1. *Facility*

Experiments were conducted in a tank 30 cm wide, 60 cm tall, 488 cm long using a semicylindrical wavemaker at one end to generate interfacial waves. Trains of progressive interfacial waves were forced over a Gaussian ridge with a standard deviation of $\sigma = 25$ cm, and with height $h_0 = 20$ cm (see figure 1*a*). The stratification is two-layer where $h_{1\infty}$ and h_2 are the lower and upper layer thicknesses. The interfacial thickness was $\delta = 1.5 \pm 0.1$ cm at the start of each experiment. A conductivity-temperature probe mounted on a vertical traverse is used to obtain density profiles to verify the initial stratification. The total water depth $h_{1\infty} + h_2$ was kept constant at 56 cm, while the height of the interface above the ridge h_r was varied between 3 and 10 cm by adjusting $h_{1\infty}$. The density difference between the two layers was varied from $\Delta\rho/\rho_0 = 2(\rho_1 - \rho_2)/(\rho_1 + \rho_2) = 1\%$ to 9%. The tank was stratified using two salt solutions. In quantitative imaging experiments, a dilute isopropyl alcohol solution was used in place of salt in the upper layer.

Interfacial waves of varied amplitude a_∞ and frequency ω can be generated. The wavemaker forcing frequency ω determines the wavenumber k_∞ in a given stratification, according to the two-layer thin-interface dispersion relation:

$$\omega^2 = gk\frac{2(\rho_1 - \rho_2)}{(\rho_1 + \rho_2)}\frac{1}{\coth(kh_1) + \coth(kh_2)}, \tag{3.1}$$

where ρ_1 and ρ_2 are the lower and upper layer densities and, away from the ridge. Additional details of the facility and the imaging set-up are described in Troy & Koseff (2005*a*).

3.2. *Measurement techniques*

The measurement techniques used in these experiments included conductivity and temperature profiles to determine the initial stratification, planar laser-induced fluorescence to provide two-dimensional density fields, and PIV to measure velocity fields. The imaging set-up is shown in figures 1(*a*) and 1(*b*). For the simultaneous PIV/PLIF measurements, a swept-beam Argon-ion system is used (e.g. Crimaldi & Koseff 2001).

3.2.1. *Scalar fields*

PLIF has been used in a wide range of flows to measure scalar concentration fields (Crimaldi 2008). In these experiments, a laser fluorescent dye (Rhodamine 6G) is added to the lower layer at a concentration of 50–80ppb. The dye in a portion of the

x–z plane is illuminated using the scanning mirror and Argon-ion laser (figure 1a). Rhodamine 6G and salt have similar Schmidt numbers, $Sc = \nu/\kappa$, 600–1200 and 700, respectively, and thus are expected to diffuse similarly (Rehmann 1996). Image pixel intensity can be converted to dye concentration and subsequently to density after appropriate calibration and correction (Crimaldi & Koseff 2001; Troy & Koseff 2005a). Images were taken at 7.5 or 15 Hz using a 1024×1024 pixel, 12-bit grey scale CCD camera (Silicon Mountain Designs), to give a typical spatial resolution of 0.2 mm (approximately the thickness of the light sheet).

The interfacial height was determined by fitting a hyperbolic tangent function to the intensity of each image column where the midpoint of the hyperbolic tangent profile is taken to be the interfacial height. This method effectively provides a wave gauge for locations visible in the image.

3.2.2. *Velocity fields*

PIV is used to obtain two-dimensional velocity data in the wave field. The Argon-ion laser is used to generate two successive light sheets, during which images of the particle field are captured using a 12-bit 2048×2048 pixel CCD camera (RedLake). MatPIV, developed by J. S. Sveen, in conjunction with the intensity capping method of Shavit, Lowe & Steinbuck (2007) is used to process the PIV images. A normalized median-residual filter is used to identify errant velocity vectors (Westerweel & Scarano 2005). Using PIV, the spatial resolution of the velocity field is 1 mm, with accuracy of ± 0.4 mm.

Simultaneous measurements of velocity and density were obtained using a PIV/PLIF system with a single laser, a scanning mirror and two cameras (Variano & Cowen 2007). During the first sweep of the laser, a PIV image was obtained. During the second sweep, a PIV image and a PLIF image were taken simultaneously. Typically, the two PIV images were separated by 3–20 ms, depending on the flow velocity, the three-dimensionality of the flow and the size of the field of view. Band-pass optical filters were used to allow the PIV camera to image the particles while blocking the signal from the dye and to allow the PLIF camera to image the dye field while excluding emissions from the particles. Simultaneous PIV/PLIF systems have been used in density-stratified flows to study the dynamics and entrainment of buoyant plumes (Law, Wang & Herlina 2003; Diez, Bernal & Faeth 2005; Ai, Law & Yu 2006). When strong density gradients are present in the flow, there are some challenges to implementing PIV/PLIF. Two salt-stratified layers will have different indices of refraction, which causes light to be distorted as it passes through density gradients in the fluid. This phenomenon can distort the appearance of the interface and can severely cloud particle and dye images of turbulent flows. In order to use PIV/PLIF in stratified flows, the index of refraction can be matched between the two layers by using a dilute solution of isopropyl alcohol in the upper layer and a salt solution in the lower layer (Daviero, Roberts & Maile 2001). For a density difference of $\Delta\rho/\rho_0 = 1\,\%$ between the layers, the index of refraction of both layers is $n = 1.3346$.

4. Results

The results from two sets of experiments are discussed in this section. In the first set of experiments, a qualitative breaking classification is developed for wave-ridge breaking events (§ 4.1), and scales of the topography and the incident wave are used to parameterize when breaking occurs (§ 4.2). The second set of experiments narrows

the focus to look just at waves on the threshold of instability. The amplitude of the incident wave is adjusted to find the lowest amplitude for which overturning is observed at the interface. Using simultaneous measurements of velocity and density, §4.3 examines whether the gradient Richardson number is a good indicator of when this onset of instability occurs.

The amplitude a is measured from fluctuations of the interfacial height in PLIF images. The wavenumber k is computed from the two-layer dispersion relation (defined in (3.1)) for a given forcing frequency of the wavemaker ω. The subscript ∞ indicates the quantity is measured or calculated just upstream of the ridge. Where k, a and h_1 appear without subscripts, the quantities are evaluated over the ridge crest.

As waves propagate up the ridge into more shallow water, the wave steepness ka tends to increase if wave energy is conserved. As the depth decreases, flow in the lower layer is constricted to a smaller vertical extent, so the magnitude of the velocity in the lower layer increases. Through some combination of increased wave steepness (i.e. increased velocity relative to the wave speed) and increased shear across the interface, waves can become unstable and break, leading to mixing. The mechanism for instability in an interfacial wave-ridge interaction is the focus of this study.

4.1. *Breaking classification*

In the breaking classification experiments, a range of waves were generated by varying the wavelength ($\lambda_\infty = 25$–300 cm), amplitude ($a_\infty = 0.5$–6 cm) and the height of the interface over the ridge ($h_r = 3$–10 cm), to vary dimensionless parameters ka, $k\delta$ and a/h_r. For the same values of ka, $k\delta$ and a/h_r, the Reynolds number was varied by a factor of 3 by changing the density difference between the layers ($\Delta\rho/\rho_0 = 1\%, 3\%, 9\%$).

Three primary types of breaking events were observed: backward breaking, forward plunging breaking and forward Kelvin–Helmholtz breaking, and examples of each breaking type are shown in figure 2. If no visible overturning was observed, waves were classified as not breaking. Backward breaking involves a counter-clockwise, shear instability in the lee of the wave crest as the wave passes over the crest of the ridge. Forward plunging breaking is characterized by a steepening of the front wave face leading to gravitational instability, qualitatively similar to the breaking of a plunging surface wave. Forward Kelvin–Helmholtz breaking involved the same convective, plunging mechanism as forward plunging breaking, but in this case, Kelvin–Helmholtz-like shear instability developed between the plunging wave face and the ridge, as strong flow rushed down slope. Qualitatively, the most vigorous wave-ridge interactions seem to result from this combination of shear and convective instability.

One striking result of the classification process was that it was not possible to classify breaking events as simply shear or convection induced breaking. Figure 3 clearly illustrates a wave breaking event with elements of convective as well as shear instability. This frame from the forward Kelvin–Helmholtz breaking event illustrated in figure 2(*c*) shows the wave face plunging downwards at the left edge of the frame, with intertwined anchor-like signatures of Rayleigh–Taylor-like gravitational instability. In the centre of the image, Kelvin–Helmholtz-like shear instabilities develop due to strong, down slope flow as the trough of the wave passes over the ridge crest, and the crest of the wave approaches from the left. Because of the mixed nature of the wave instability in many of the observed breaking events, established instability criteria for shear or convective regimes become difficult to apply.
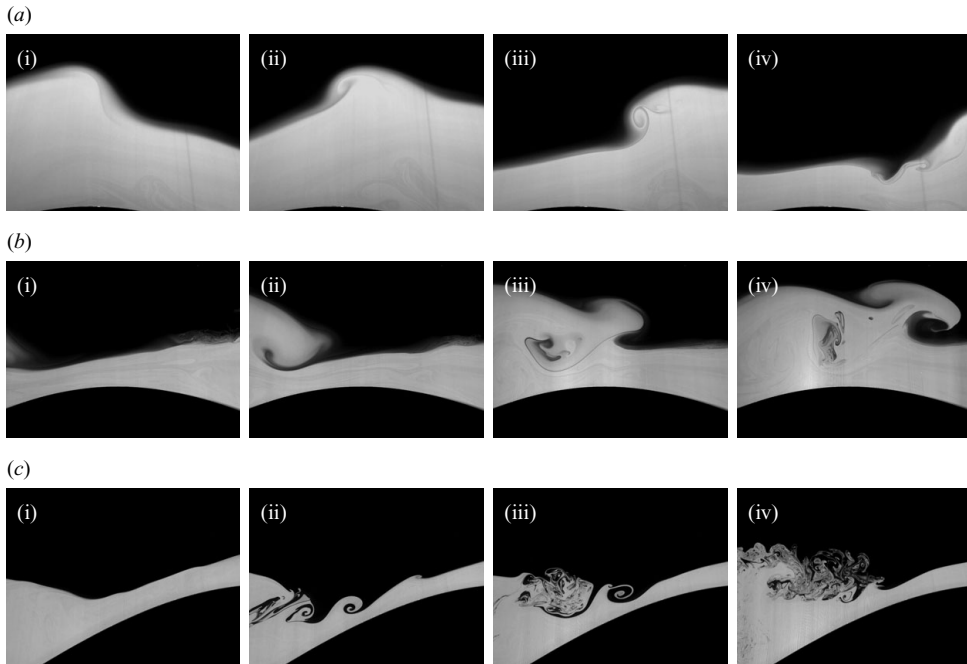
(a)

(b)

(c)

FIGURE 2. PLIF images showing breaking types: backward breaking (a), forward plunging breaking (b) and forward Kelvin–Helmholtz breaking (c). Waves propagate left to right. The dark region at the bottom of images is the ridge.

FIGURE 3. Interaction of shear and convection in wave instability. Reprinted with permission from (Hult, Troy & Koseff 2006). Copyright 2006, American Institute of Physics.

4.2. *Parameterization of breaking types*

The breaking mechanism can be predicted, to a degree, using scales of the incident wave and topography. The relevant scales are the incident wave amplitude (a_∞), the length scale of the wave (k_∞^{-1}), the height of the interface above the ridge crest (h_r)
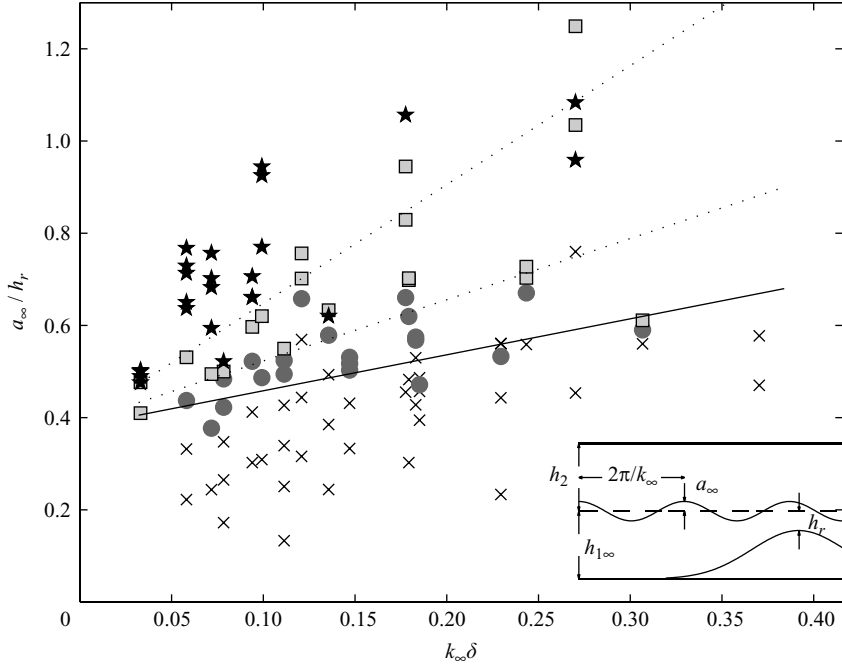
FIGURE 4. Breaking classification for periodic, interfacial waves at a Gaussian ridge. Solid line (-) shows the transition to breaking and dotted lines, (..) suggest breaking regimes. Symbols indicate breaking type: forward Kelvin–Helmholtz breaking ($\star$), forward plunging breaking ($\square$), backward breaking ($\bigcirc$), not breaking ($\times$).

and the interface thickness (δ). Figure 4 shows that the breaking regimes can be parameterized by the scaled amplitude a_∞/h_r and the scaled wavelength $k_\infty\delta$. The breaking transition curve (solid) and the breaking type curves (dotted) are fit to minimize the root mean square distance of points on the wrong side of each curve. The solid curve provides an empirical breaking criterion defined by a_∞/h_r and $k_\infty\delta$ for the range of parameters tested. In the limit of very long or very short waves, or when the topography is exceedingly steep, this breaking criterion may not hold. Dotted lines are intended to suggest regions where a given breaking type tends to occur. For a constant value of $k_\infty\delta$, as the amplitude a_∞/h_r was increased waves tended to first break backwards, then forwards. Waves may be unstable to backward breaking while stable to forward breaking due to the effects of interfacial shear. This is because as a wave shoals, the increasing interfacial shear at the crest is opposed by the steepening of the wave face. When the wave reaches the crest of the ridge, however, wave steepening ceases and the interfacial shear can cause the wave to become unstable. Forward Kelvin–Helmholtz breaking tended to occur when a_∞/h_r was high and the scaled wavenumber was low, i.e. when waves were steep and long relative to the interface thickness. For very short waves ($k_\infty\delta > 0.3$), wave breaking was observed, but the specific breaking mechanisms seemed to be heavily dependent on perturbations from previous wave-ridge interactions and events were not very repeatable. The results of this parameterization do not vary significantly when the Reynolds number was increased by a factor of 3 from $Re = 200$–7000 to $Re = 600$–$20\,000$ for the same values of a_∞/h_r and $k_\infty\delta$.

Experiment	f (Hz)	λ_∞ (cm)	a_∞ (cm)	Stability
2	0.0375	295	0.76	Stable
3	0.0375	295	0.83	Overturing
4	0.0375	295	0.72	Stable
5	0.050	212	1.26	Stable
6	0.050	212	1.43	Stable
7	0.050	212	1.51	Borderline
8	0.050	212	1.60	Overturning
9	0.075	123	1.52	Borderline
10	0.075	123	1.66	Overturning
11	0.075	123	1.37	Stable
12	0.100	76	1.95	Stable
13	0.100	76	2.17	Borderline
14	0.100	76	2.39	Overturning
15	0.125	50	2.65	Stable
16	0.125	50	2.89	Borderline
17	0.125	50	3.13	Overturning

TABLE 1. Parameters for Ri_g experiments.

4.3. *Shear instability criterion*

This section takes a closer look at the flow conditions in waves at the threshold of initial instability. The key questions are What is the mechanism that initially leads to instability as the wave steepness is increased? and Is there a dynamic criterion to predict when this instability occurs in the wave-ridge case? To investigate the utility of the $Ri_g > 0.25$ stability criteria for this case of interfacial waves breaking at a ridge, simultaneous PIV/PLIF was used to determine the minimum value of Ri_g that occurs at the onset of wave instability. Waves of varied wavenumber k_∞ were forced over the ridge and the wave amplitude was increased until overturning was observed (see table 1). For all Ri_g experiments, $h_r = 5$ cm and $\Delta\rho/\rho_0 = 1\%$. Each experimental run contained five consecutive periodic waves of constant amplitude. Between experimental runs, the two-layer stratification was sharpened.

Figure 5 shows the evolution of the interface for several waves events at the threshold of instability with varied wavelength. The contours of the mean density ($\rho = 999.7$ kg m^{-3}) illustrate fluctuations of the density interface as a wave passes over the ridge crest. As t/T increases, first the trough of the wave passes over the ridge at $t/T \approx 0.4$, followed by the crest of the wave at $t/T \approx 0.6$–0.8. The breaking events shown in figures 5(*c*), 5(*d*) and 5(*e*), are qualitatively similar to the event shown in figure 2(*a*). In these events, the wave steepens as it passes over the ridge crest and then overturns backwards in the lee of the wave crest. In figures 5(*a*) and 5(*b*), when the waves are long relative to the interface thickness and the ridge, ($k_\infty\delta < 0.06$), incipient overturning is observed for much less steep waves. For these two cases, flow separation at the bed may provide an alternative mechanism contributing to initial instability and this mechanism is discussed in §4.4.

4.3.1. *Calculating Ri_g*

From density and velocity profiles, Ri_g is calculated as a function of x, z and time. Figure 6 shows sample profiles of N^2 and $(\mathrm{d}u/\mathrm{d}z)^2$ and the evolution of Ri_g in the column of water directly over the ridge crest throughout the wave period. In a two-layer flow, overturning must occur in the density interface in order to mix the stratifying scalar, and thus we are interested in whether there is a critical value
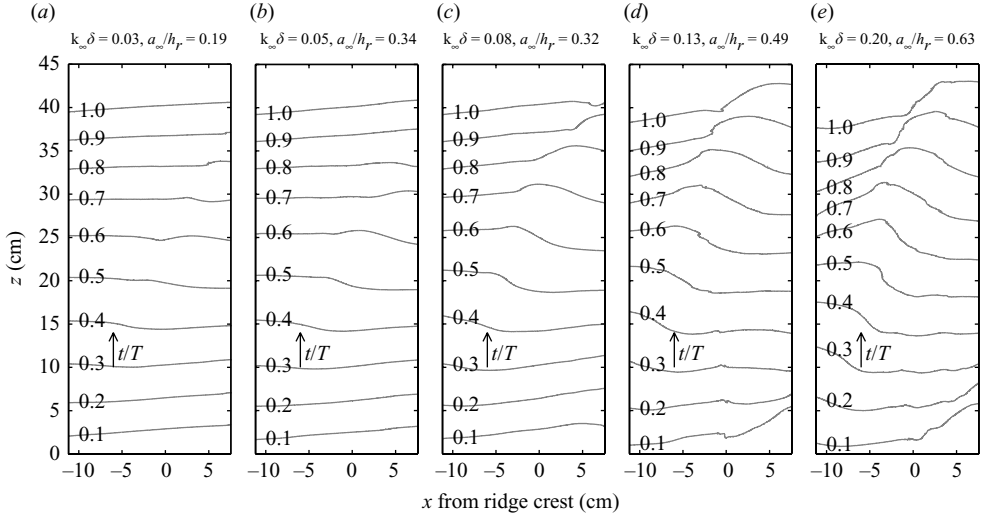
FIGURE 5. Evolution of the contour of mean density ($\rho = 999.7$ kg m^{-3}) over the ridge. Contour labels are t/T where T is the wave period. The y-axis shows an arbitrary height z.
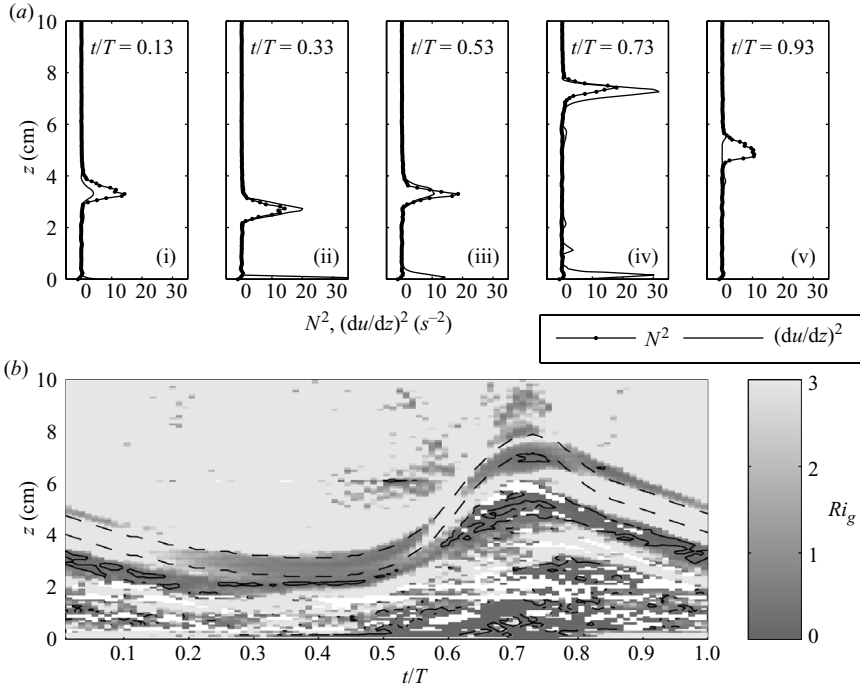

FIGURE 6. (*a*) Profiles are shown of N^2 and $(\mathrm{d}u/\mathrm{d}z)^2$ over the ridge crest for five points in the wave period T. In (*a*) and (*b*), z is distance above the ridge crest. In (*b*), contours of $Ri_g(z, t)$ over the ridge crest are shown as a function of t/T. Black contours show $Ri_g = 0.25$ and dashed contours bound the density interface. For this event (also shown in 5*c*), $k_\infty \delta = 0.082$ and $a_\infty/h_r = 0.32$.

for Ri_g within the interfacial region for instability. The interfacial region is defined here based on distance from the mean density value contour. Away from the density interface, noise in the density measurements tends to dominate the calculated values of Ri_g. White patches below the interface in figure 6 are due to dye irregularities in the lower layer which cause non-physical negative values of Ri_g. The thickness of the region about the mid-density contour was chosen to be as large as possible without including the regions above and below the density interface, where noise dominates the measured density gradients. For these experiments, the interfacial region is defined to be 3 mm below to 5 mm above the mean density contour, which typically contains 80 % of the density variation. The sensitivity of the results to this definition was less than measurement uncertainty ($Ri_g \pm 0.1$ within the interface, $Ri_g \pm 1$–10 elsewhere).

The profiles shown in figure 6(a) show that the magnitude of the stratification N^2 stays approximately constant over the wave period, while the magnitude of the shear, $(du/dz)^2$, varies significantly, with peak values at the wave crest (figure 6a, image (iv)) and trough (figure 6a, image (ii)). These observations are typical of the shoaling waves observed. In figure 6(b), patches of low Ri_g occur in the interfacial region when the crest and trough of the wave pass over the ridge crest.

4.3.2. *Evolution of* Ri_g

Figure 7 shows a time series of the minimum Ri_g in the water column directly above the ridge crest as the trough and then the crest of the wave pass by. For all wavelengths, two local minima in Ri_g are present: during the trough and crest of the wave when shear across the interface is highest. The minimum of Ri_g during the trough typically persists longer, although overturning occurred as the crest of the wave passed the ridge.

The minimum value of Ri_g within the density interface is plotted in figure 8 for each wave. A transition occurs from stable to overturning when $(du/dz)^2$ is of the order of N^2, i.e. $0.2 < Ri_{g,min} < 0.4$, with measurement uncertainty of ± 0.1. Possible factors impacting the variability of the critical Ri_g are discussed later in this section. Once overturning occurs, Ri_g may be negative. Note, the values of $Ri_{g,min}$ in figure 8 are typically smaller than the minimum value over the wave period shown in figure 7, where $Ri_{g,min}(t/T)$ is averaged over five wave events of equivalent a_∞/h_r. There is a discrepancy between local and phase averaged data because the minimum value of Ri_g during the wave period does not always occur at precisely the same phase of the wave. Taking the minimum value in a noisy data set will likely bias the resulting critical value to be too low, but within the uncertainty indicated.

At first glance, figure 8 suggests $Ri_{g,min} = 0.25$ provides a reasonably good cutoff for when interfacial waves first become unstable. However, the minimum values of Ri_g shown in figure 8 do not always occur during the crest of the wave, where overturning is observed. Because the ridge acts to vertically constrain flow in the lower layer to a greater extent while the trough passes than when the crest passes, the minimum Ri_g is expected to occur during the trough. If shear alone causes the instability, we would expect the instability to develop in the trough of the wave. Since overturning is observed at the crest of the wave, shear must not be the only factor, suggesting convective acceleration may also play a role in the wave instability.

Both shear and convection appear to contribute to initial instability at the wave crest, as the wave steepness is increased. The wave amplitude scaled by the minimum lower layer depth over the ridge a/h_r provides a measure of the wave nonlinearity, and in the limit of highly nonlinear shoaling waves when a/h_r is large, convective instability is expected. Figure 9 indicates that while low Ri_g is often present for waves
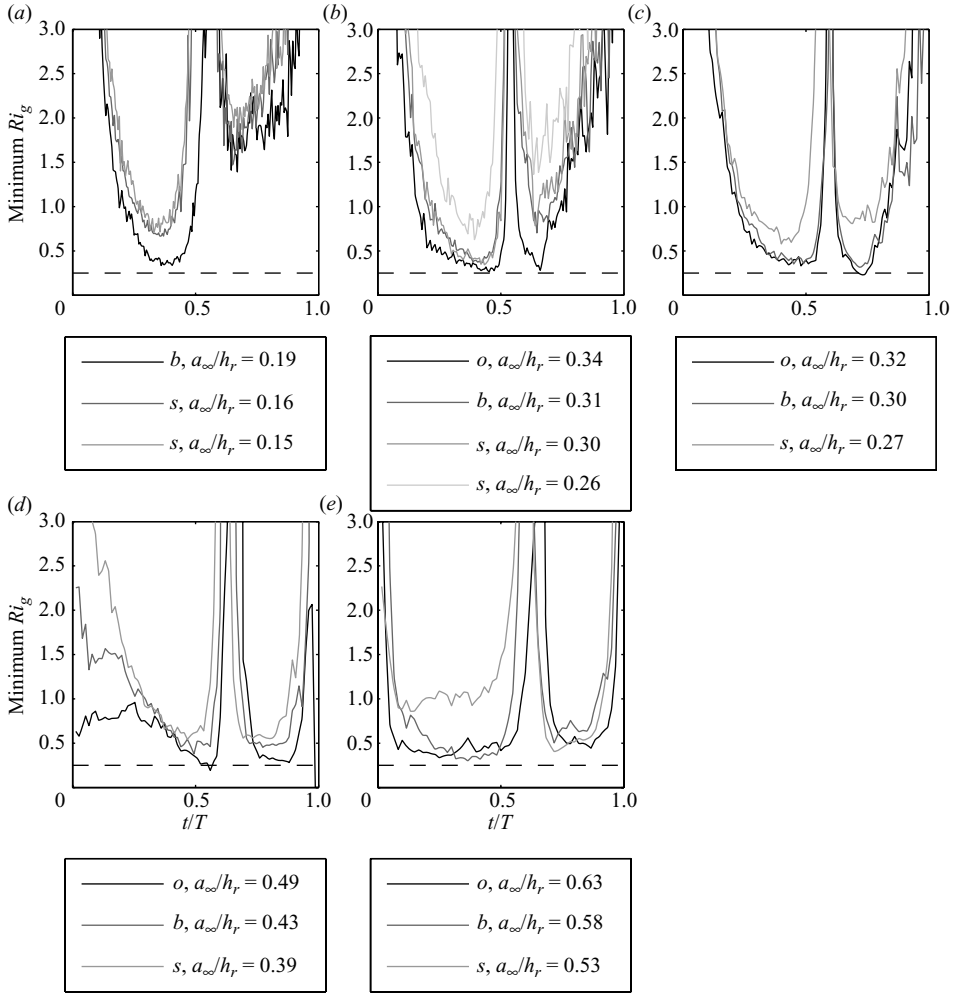
FIGURE 7. Minimum value of Ri_g in the water column, directly over the ridge crest over the wave period. Here, 'o' indicates overturning, 'b' is borderline and 's' is stable. For (a) $k_\infty \delta = 0.034$, (b) $k_\infty \delta = 0.048$, (c) $k_\infty \delta = 0.082$, (d) $k_\infty \delta = 0.132$ and (e) $k_\infty \delta = 0.202$. The phase t/T corresponds with that at $x = 0$ in figure 5. At $t/T = 0$, the interface deflection is zero, then the wave trough ($0 \leqslant t/T \lesssim 0.5$) passes followed by the crest ($0.5 \lesssim t/T \leqslant 1$).

at the onset of instability, high scaled amplitude a/h_r is also present. Note, in figure 9, a is the local amplitude over the ridge crest. The results in figure 9 the critical value of Ri_g for breaking is sensitive to the local wave nonlinearity a/h_r. The results of Troy & Koseff (2005b) indicate that in the absence of a shoaling slope, the breaking transition occurs at $Ri_g \approx 0.1$, for waves of comparable $k_\infty \delta$ and a_∞/h_r that were forced to break in a channel contraction. In this study, the wave nonlinearity a/h_r is increased, and this seems to increase the critical Ri_g from 0.1. When $a/h_r > 0.4$, the steady parallel shear stability criterion of $Ri_g > 0.25$ clearly does not hold. This supports the notion that the instability is initiated by a combination of shear and convection in these wave-ridge interactions. Separation induced breaking events mark another topographic process that can lead to overturning when $Ri_g > 0.25$.
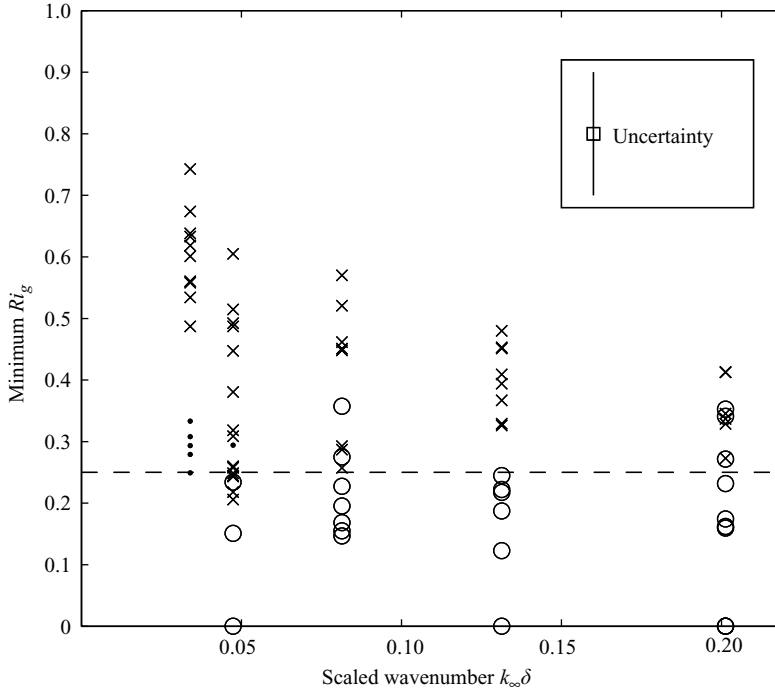
FIGURE 8. Dashed line indicates $Ri_g = 0.25$. Symbols denote wave stability: stable (x), separation breaking (●) and backward breaking (○). If $Ri_g < 0$, Ri_g is plotted at 0.

For waves shorter relative to the topography (higher $k_\infty\delta$), the critical waves are steeper, thus the interaction with the ridge is more nonlinear. The assumptions of parallel and steady flow required for the $Ri_{g,min} > 0.25$ stability criterion become less appropriate as $k_\infty\delta$ increases. Figure 10 shows a measure of nonlinearity: the maximum values of u/c and w/c over the wave period where c is the phase speed of the wave over the ridge, $c = \omega/k$. Note that while u/c_{max} is relatively constant for the range of $k_\infty\delta$ tested, the vertical velocity w/c_{max} varies with $k_\infty\delta$ for near-breaking waves. For $k_\infty\delta > 0.2$, w/c_{max} is of the same magnitude as u/c_{max}. Larger convective accelerations for $k_\infty\delta = 0.20$ may lead to overturning at slightly higher values of Ri_g in figure 8, following from the results of Fringer & Street (2003) which found that as $u/c \to 1$ for shorter waves, stability is governed by convective processes rather than interfacial shear. Note that the breaking criterion of $u/c > 0.7$ discussed by Sveen *et al.* (2002) for internal solitary waves at a ridge does not predict breaking in this periodic wave case.

Another factor that may increase scatter in the results in figure 8 for shorter waves (higher $k_\infty\delta$) is the role of random perturbations to the initial interface. For shorter waves relative to the ridge, interfacial disturbances have less time to propagate from the breaking location over one wave period, making shorter waves more sensitive to previous events. Interface disturbances from previous breaking events can be seen in figures 5(*d*) and 5(*e*), and may contribute to instability of the current wave.

4.4. *Separation of wave-induced boundary layer*

When the wavelength is long relative to the ridge ($k_\infty\delta \lesssim 0.06$), an alternative mechanism may lead to instability of the interface. When the scaled amplitude

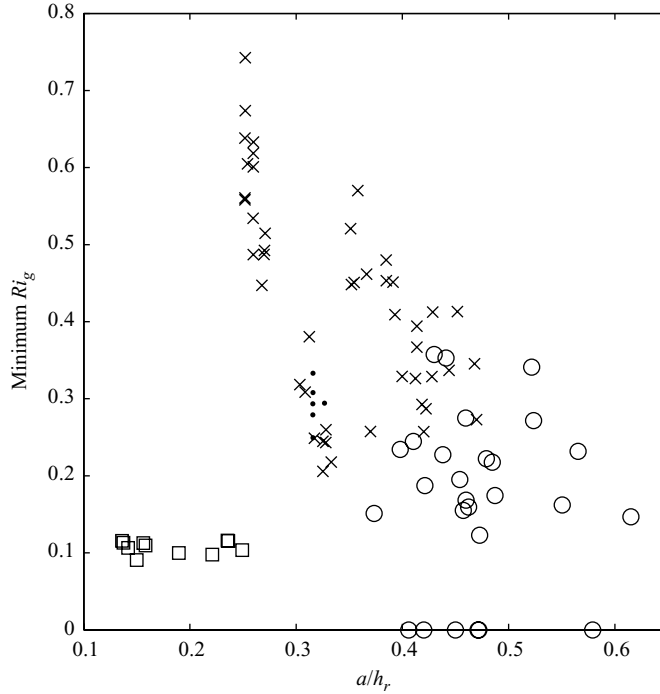FIGURE 9. Ri_g versus a/h_r for the experiments on waves at the onset of instability. Symbols denote wave stability: stable ($\times$), separation breaking ($\bullet$), backward breaking ($\circ$) and points at the onset of breaking in data adapted from Troy & Koseff (2005*b*) ($\square$). If $Ri_g < 0$, Ri_g is plotted at 0.
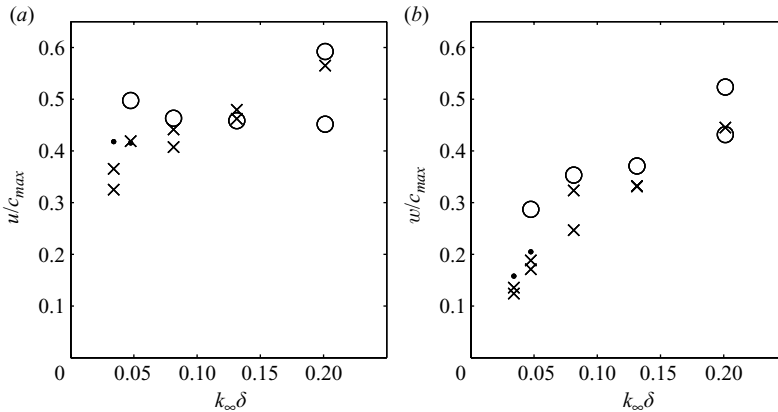

FIGURE 10. Maximum velocity (u,w) as a fraction of the phase speed of the wave c. Symbols denote wave stability: stable ($\times$), separation breaking ($\bullet$) and backward breaking ($\circ$). In this figure, velocities are from the ensemble average of six successive wave events.

a_∞/h_r is increased, the first instance of overturning at the interface may be caused by separation of the wave flow over the ridge. This phenomenon of separation at the bed under a passing internal wave has been observed in numerical simulations (Diamessis & Redekopp 2006) and in experiments in the laboratory (Carr & Davies 2006; Carr, Davies & Shivaram 2008). Thorpe (1998) proposed a separation vortex
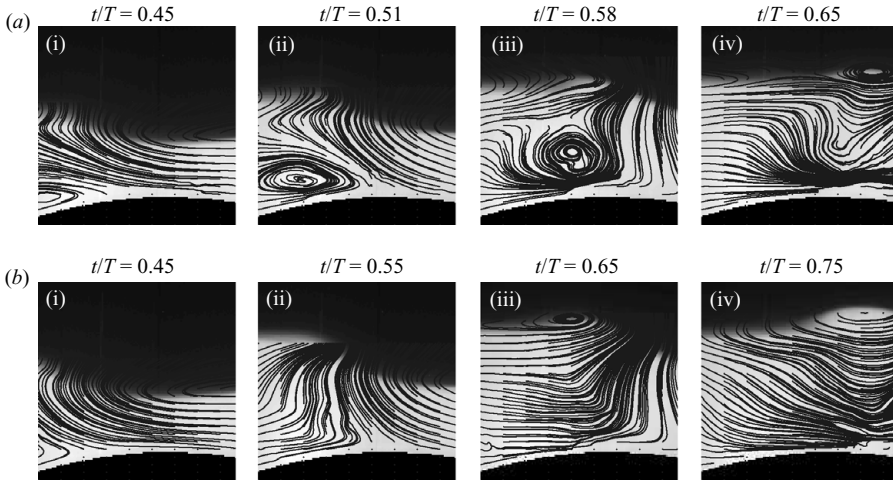
FIGURE 11. Black lines show instantaneous streamlines based on the measured velocity field in the lower layer. In (*a*), $k_\infty \delta = 0.048$, $a_\infty / h_r = 0.34$. In (*b*), $k_\infty \delta = 0.082$, $a_\infty / h_r = 0.323$.

would develop beneath a shoaling internal solitary wave, and such vortices have been observed in the ocean (Bogucki, Dickey & Redekopp 1997) and in the lab (Thorpe 1998). As the trough of the wave passes over the ridge, strong flow to the left in the lower layer tends to detach from the ridge and a separation vortex is formed just upstream of the ridge crest. Instantaneous streamlines in figure 11(*a*), images (i) and (ii) show the development of this separation vortex. As the crest of the wave passes the ridge, the vortex is lifted from the bed and is advected downstream in images (iii) and (iv), unlike in previous solitary wave studies such as Boegman & Ivey (2009). This vortex coincides with an interfacial disturbance which eventually overturns. This lifted vortex may help to explain why the wave crest becomes unstable when $Ri_g > 0.25$, as shown in figures 7(*a*) and 7(*b*). When the wavelength is shorter relative to the topography, i.e. $k_\infty \sigma \gtrsim 1$, this separation vortex is not observed, as shown in figure 11(*b*). Note, the streamlines in figure 11 are instantaneous and in a highly unsteady flow such as this, particles in the flow will not follow streamlines. In this complex wave-bathymetric interaction, it is difficult to tease out exactly the contributions of each type of instability observed. As the wave amplitude is increased, the wave breaking intensifies and it becomes increasingly difficult to distinguish the role of separation at the bed and instability at the interface. Figure 12 shows the velocity field during a plunging wave event, with vortices developing in the lower layer.

Diamessis & Redekopp (2006) argue that if the Reynolds number and amplitude are sufficiently large and an adverse pressure gradient is applied over a long enough time, the separation bubble under the wave can become unstable and then periodically eject vortices into the water column. In this study, no vortices were observed to be ejected from the separation bubble, but in the long wave limit, this may be possible. Unlike previous solitary wave studies, though, the separation vortex itself appears to be lifted into the water column here. Both the coherence of the lifted separation vortex observed in this study and the tendency for separation bubbles to eject vortices are sensitive to *Re*. Therefore, the impact of such vortices on interfacial stability will depend on *Re*. While this bed separation may not lead directly to the instability of
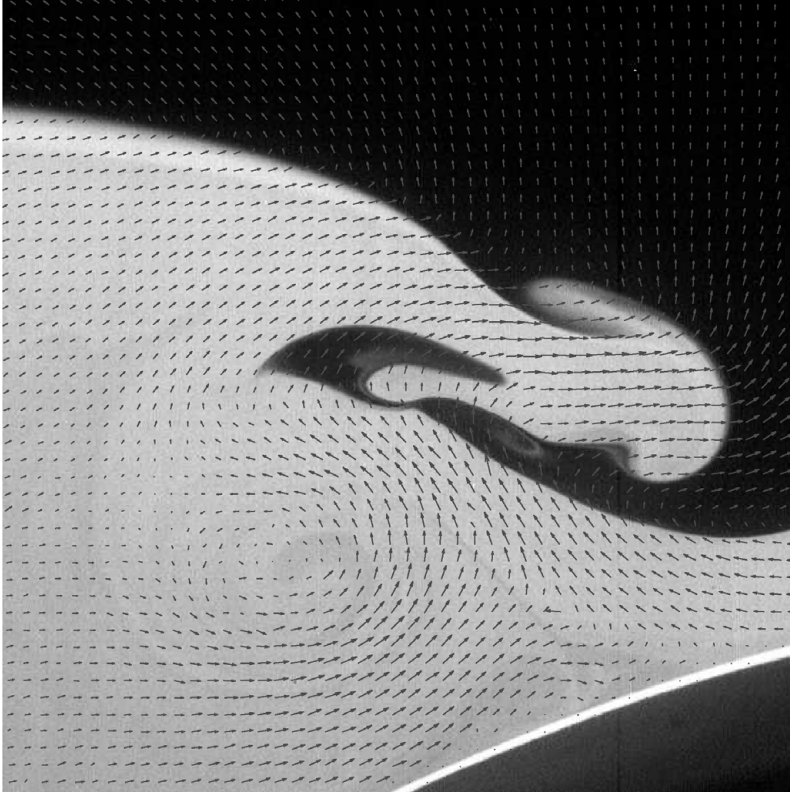
FIGURE 12. Velocity vectors overlayed on PLIF image for a plunging wave. For this case,
$k_\infty \delta = 0.082$, $a_\infty / h_r = 0.70$.

the wave face, the vortex may enhance resuspension of bed sediments under the wave, as suggested by Diamessis & Redekopp (2006) and Boegman & Ivey (2009).

5. Discussion

It is clear that interfacial shear plays an important role in the wave breaking events in this study. Although an Ri_g criterion is arguably an insufficient tool to assess stability in an unsteady, nonlinear flow such as this, it is commonly applied to internal wave flows and mixing parameterizations in stratified flows. The shear instability metric Ri_g can be very difficult to measure, however, even under idealized laboratory conditions. In §5.1, a simple model is presented to estimate the expected Ri_g using only the wave parameters and topography. The model is compared with experimental results, and then used to assess various predictive breaking criteria. Whether or not these predictive criteria can be used to distinguish the wave breaking mechanism is also discussed. In §5.2, the role of unsteadiness is discussed.

5.1. *Modified Ri model*

A simple linear model for wave flow over the ridge can be developed by modifying the theoretical wave Richardson number Ri_w analysis of Troy & Koseff (2005*b*) to include the effects of finite layer depths. Troy and Koseff form the wave Richardson number in terms of a scaled amplitude and scaled wavenumber for a low-mode

progressive, interfacial wave in two deep layers:

$$Ri_w \equiv \frac{N^2}{\left|\frac{\partial U}{\partial z}\right|^2}|_{z=o,x=crest/trough}, \tag{5.1}$$

$$Ri_w \approx \frac{g(\rho_1 - \rho_2)/(2\delta/5.3)}{(\rho_0)((\Delta u)/(2\delta/5.3))^2} \approx \frac{k\delta}{5.3(ka)^2}, \tag{5.2}$$

where the constant 5.3 arises from the definition of the interfacial thickness. The approximation for Δu across the interface can be modified to include the effects of variable depth layers, starting from the two-layer lowest mode interfacial wave solution for the horizontal velocity within each layer (e.g. Phillips 1966):

$$u_1(x, z, t) = a\omega \frac{\cosh(k(z + h_1))}{\sinh(kh_1)} \cos(kx - \omega t), \tag{5.3}$$

$$u_2(x, z, t) = -a\omega \frac{\cosh(k(z - h_2))}{\sinh(kh_2)} \cos(kx - \omega t). \tag{5.4}$$

The velocity maximum occurs at the interface ($z = 0$) during the crest and the trough, so the maximum velocity difference across the interface is

$$\Delta u_{max} = a\omega(\coth(kh_1) + \coth(kh_2)). \tag{5.5}$$

The two-layer finite depth dispersion relation (defined in (3.1)) is substituted to obtain a modified wave Richardson number for the case of finite layer depths:

$$Ri \approx \frac{k\delta}{2.65(ka)^2} \frac{1}{(\coth(kh_1) + \coth(kh_2))}. \tag{5.6}$$

This modified wave Richardson number provides an estimate of the minimum Ri_g for periodic interfacial waves in terms of the wave steepness ka, the scaled wavenumber $k\delta$ and the scaled layer depths kh_1 and kh_2. For the deep water case when $kh_1 \gg 1$ and $kh_2 \gg 1$, this expression converges to the result in (5.2). This model does not include the effects of abrupt changes in depth, boundary layer effects, or finite amplitude effects on the velocity field near the interface. To this effect, the model assumes the peak shear occurs at the middle of the density interface where N^2 is maximum. At the limit where the wave steepness is increased to the point where wave-ridge interactions result in overturning, this model will not accurately predict Ri.

A time-varying wave Richardson number can be calculated by preserving the time variation in the velocity

$$\Delta u_{x=const} = a\omega \left(\coth(kh_1) + \coth(kh_2)\right) \cos(\omega t), \tag{5.7}$$

and then which gives a time-varying wave Richardson number

$$Ri(t) \approx \frac{k\delta}{2.65(ak)^2 \left(\coth(kh_1) + \coth(kh_2)\right) \cos^2(\omega t)}. \tag{5.8}$$

Again, this time-varying estimate does not include the effects of steep topography, boundary layers or finite amplitude waves.

5.1.1. *Comparison of data and model results*

Figure 13 compares the measured minimum Ri_g with the modelled $Ri(t)$ from (5.8). The expression for $Ri(t)$ in (5.8) does not include finite amplitude effects on the velocity field over the ridge, which leads to the difference in the magnitude of Ri_g
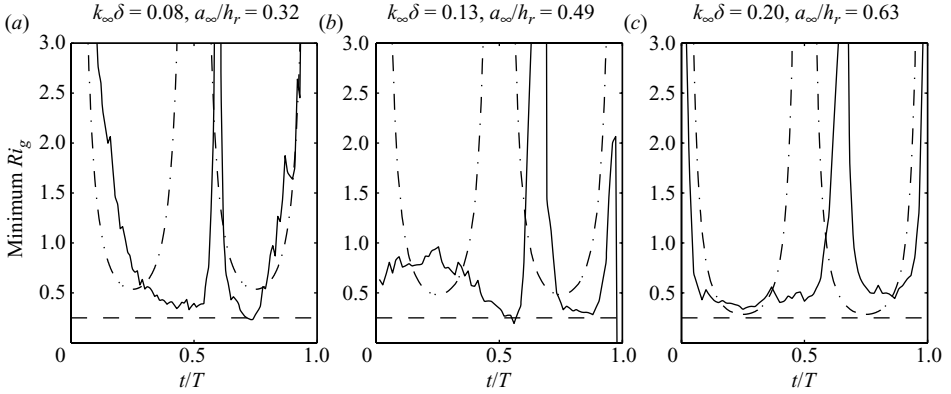
FIGURE 13. $Ri(t)$, directly over the ridge crest. Experimental data (——) and the $Ri(t)$ theory (.-.). Here, $h_r/\delta = 3.3$.

between the trough and the crest in the experimental data. For the longest waves ($k_\infty\delta < 0.06$), the model sharply overpredicts the minimum Ri_g during the trough of the wave ($0 \leqslant t/T \lesssim 0.5$). For shorter waves, the agreement between the model and the observations is better. Generally, the measured data indicate the flow over the wave period is noticeably more complex than the model predicts. Despite variation, the results in (5.8) suggest that if the wavelength, amplitude, stratification and topography are known for a near-critical progressive periodic interfacial wave, the minimum Ri_g can be predicted to within a factor of 2 by this model for waves where flow separation does not occur.

5.1.2. *Comparison of breaking criteria*

Two main breaking criteria have been presented in this study: an empirical breaking condition based on incident wave and topographic scales (figure 4), and a Ri_g breaking condition. These two breaking criteria are not independent. The empirical shoaling criterion simply indicates when the transition to breaking was observed in the experiments, without regard to the particular breaking mechanism. Whereas, an Ri_g condition indicates when shear may cause a flow to become unstable. The relevance of these two criteria depend on the particular flow under consideration, as there are cases when each criterion is more appropriate. For example, a shoaling criterion based on a changing depth is not relevant to periodic interfacial waves passing through a contraction in the channel width break, but waves did break at $Ri_g \approx 0.1$ (Troy & Koseff 2005b). On the other hand, surface waves at a beach are unlikely to break due to interfacial shear at the air–water interface, but breaking criteria based on a/h have been widely validated for this case. Figure 9 also highlights the relative importance of shear and wave nonlinearity.

To compare the predictive capability of the empirical shoaling criterion shown in figure 4 and an Ri_g criterion for the waves of this study, both criteria were rewritten in terms of incident wave parameters (k_∞, a_∞) and scales of the bathymetry and stratification (h_1, h_2, h_r, δ). Figure 14 shows how these two criteria compare for the deep water waves of Troy & Koseff (2005b) in figure 14(a) as well as for two lower layer depths over the ridge shown in figures 14(b) and 14(c). The model in (5.6) is used to find the critical wave steepness ka associated with $Ri_g = 0.25$. Because the wave Richardson model requires a constant of proportionality related to
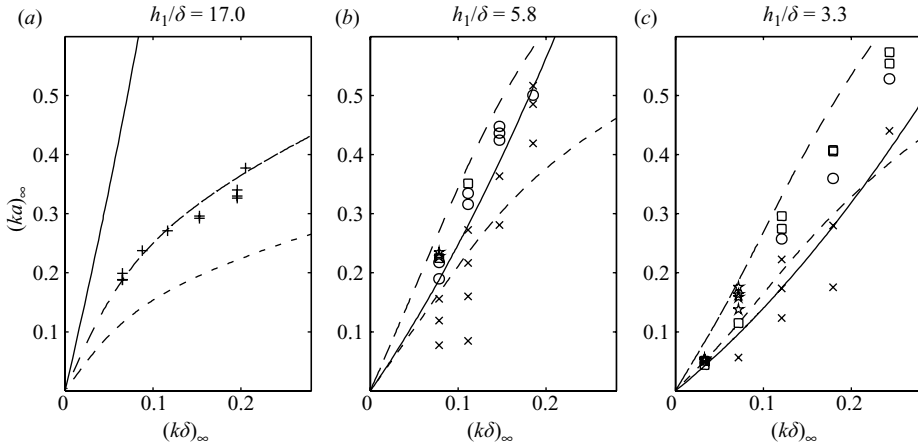
FIGURE 14. Three cases comparing the empirical shoaling criterion from (5.9) (—), and two estimates of $Ri = 0.25$ based on $ka = (8k\delta/5.3)^{1/2}(\coth(kh_1) + \coth(kh_2))$ (.-.) and $ka = (4k\delta)^{1/2}(\coth(kh_1) + \coth(kh_2))$, where linear shoaling is assumed to find k_∞ and a_∞ from k and a over the ridge. The deep water case is shown in (a) including data adapted from Troy and Koseff (2005), $+$ indicating waves at the onset of instability. Two ridge cases are shown: in (b) $h_1 = 10 cm$ over the ridge and in (c) $h_1 = 6 cm$. For (b) and (c), $\sigma = 25$ cm. Symbols in (b) and (c) indicate breaking type: forward Kelvin–Helmholtz breaking ($\star$), forward plunging breaking ($\square$), backward breaking ($\bigcirc$), not breaking (x).

the definition of the interfacial thickness (Troy & Koseff 2005b), two estimates for the $Ri_g = 0.25$ shear criterion are shown: $ka = (8k\delta/5.3)^{1/2}(\coth(kh_1) + \coth(kh_2))$ and $ka = (4k\delta)^{1/2}(\coth(kh_1) + \coth(kh_2))$. For simplicity, conservation of wave energy and linear shoaling is assumed to relate k and a over the ridge to incident wave values k_∞ and a_∞. The empirical shoaling criterion corresponds to the curve in figure 4 that separates breaking from non-breaking waves and is a function of $k_\infty\delta$ and a_∞/h_r. It can be rewritten as

$$(ka)_\infty = 0.78(k_\infty\delta)^2\frac{h_r}{\delta} + 0.38(k_\infty\delta)\frac{h_r}{\delta}. \tag{5.9}$$

From figure 14, it can then be determined which breaking criterion will be exceeded first as the wave steepness (ka) is increased, using only scales of the incident wave, topography and stratification. Figure 14 is designed to show how these criteria can be used to predict breaking behaviour, so the data and criteria are plotted in terms of incident wave scales.

For the deep water case in figure 14(a), the shear criterion will be exceeded before the effect of the bottom becomes important, making the empirical shoaling criterion irrelevant. This is consistent with the findings of Troy & Koseff (2005b) who observed waves breaking through shear instability at the wave crest and trough as they steepened when passing through a horizontal contraction in the tank. For the two ridge cases in figures 14(b) and 14(c), the shear criterion curves and the empirical shoaling curve fall within the same region of the parameter space. This suggests that for the ridge cases, the shear criterion and the empirical shoaling criterion provide similar predictive capability for the transition to breaking.

Although figure 7 indicates that the agreement between the estimated Ri_g and the experimental data is not perfect, the estimated Ri_g is sufficient to show that for the ridge cases figures 14(b) and 14(c), the empirical shoaling criterion is roughly a

curve of constant Ri_g. While unsteadiness and wave nonlinearity can alter the critical value of Ri_g, Fringer & Street (2003) suggest that an unsteady wave flow breaking at a constant Ri_g can indicate that shear is responsible for wave breaking. For the wave-ridge interactions in this study, low values of Ri_g are correlated with high values of a/h_r, as shown in figure 9, although this is not universally true. A correlation is also seen between Ri_g and the empirical shoaling criterion because the empirical shoaling criterion depends strongly on a/h_r over the ridge (figure 4). Because low Ri_g and high-wave nonlinearity are correlated for the parameters used in this study, it is difficult to distinguish the impact of interfacial shear from the impact of wave steepness on the initial wave instability.

5.2. *Unsteadiness*

In time-varying flows, critical shear must be applied for sufficient time in order for shear instability to develop (Troy & Koseff 2005b). If the time the wave shear is applied, τ_w, is long relative to the time scale for instability growth (τ_g), the unsteadiness of the flow is not likely to restrict instability growth. Kao *et al.* (1985) used a simple scaling to compare these time scales. The instability growth rate is assumed to be linearly proportional to the maximum shear, so the ratio of time scales is

$$\frac{\tau_w}{\tau_g} \approx \frac{\omega^{-1}}{(\partial u/\partial z_{max})^{-1}} \approx \frac{\Delta u_{max}}{(\omega\delta)}. \tag{5.10}$$

If Δu_{max} is calculated from (5.7), under these assumptions, the time scale ratio is $3 < \tau_w/\tau_g < 9$ for all waves in this study, suggesting that shear instability growth may be limited by the effects of unsteadiness. It has been shown, however, that the instability growth rate is not simply proportional to the maximum shear, but instead is a function of Ri as well as the length scale of the perturbation to the flow, for parallel inviscid steady shear flow (Hazel 1972). Following Troy & Koseff's (2005b) application of Hazel's result, the instability growth rate can be modelled as

$$\sigma_i = \frac{2.65\Delta u_{max}}{\delta}(-0.8Ri_0 + 0.2), \tag{5.11}$$

and then the growth can be integrated over the time subcritical shear is present. This is the growth rate for the most unstable perturbation, although in this case, the length scale of the ridge may impact the wavelength of the instability. For the waves at the threshold of instability discussed in §4.3, the minimum values of Ri_g are not substantially below $Ri_g = 1/4$. Therefore, the growth rates calculated using (5.11) for waves on the threshold of instability are near zero. If a near-zero growth rate is used for τ_g^{-1}, the wave time scale is much shorter than the instability growth rate. This analysis would then suggest that there is not sufficient time for an instability to develop in cases where overturning was indeed experimentally observed. As stated earlier, shear and convection both seem to have a role in the initial instability. Because of this, the instability growth rates for parallel inviscid steady shear flow may not in fact be appropriate. While two imperfect growth rate estimates suggest that the unsteadiness of the wave flow may inhibit instability development, the exact growth rate for this case is unknown.

The unsteadiness of the wave flow can also inhibit the development of a gravitational instability, as illustrated in figure 15. Some of the larger amplitude wave breaking events appear to involve gravitational instability, such as figure 2(b). As the wave face steepens and the crest of the wave accelerates out ahead of the wave, the overhanging mass of denser water is gravitationally unstable. At this point, the
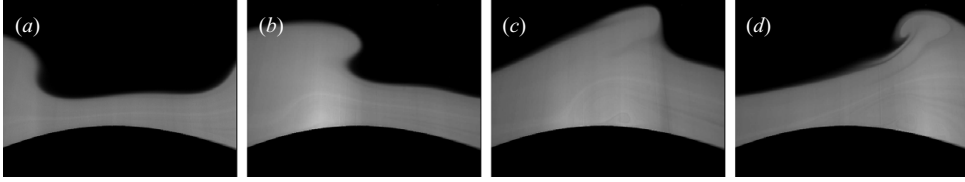
FIGURE 15. PLIF images from a wave breaking event $k_\infty\delta = 0.23$.

denser fluid may plunge downwards, resulting in turbulence and mixing. In this case, the relevant time scales are the wave time scale and the growth rate for gravitational instability. If the wave phase changes before the dense fluid can plunge downwards, the wave may not become unstable. Often the criterion of $u/c > 1$ is used to determine whether convective breaking is occurring. There are, however, cases where the flow is gravitationally unstable in one instant, but this does not lead directly to instability and convective breaking, as shown in figure 15. In this wave event, there are clearly instantaneous unstable density profiles and locations where the local velocity exceeds the phase speed of the wave, but the wave face ultimately does not plunge downwards. Although conditions for convective instability are not investigated in great detail in this study, observations indicate that $u/c > 1$ is not a sufficient criterion for instability in this case.

6. Conclusions

Laboratory experiments have been used to investigate the breaking of progressive periodic interfacial waves at a Gaussian ridge. The results clearly indicated that both shear and convection played a role in the breaking events. Because both shear and convective processes contributed to wave breaking, neither a shear instability criterion nor a convective instability criterion such as $u/c > 1$ was appropriate for all cases observed. Three types of breaking were observed: backward breaking, convective forward plunging breaking and a mixed convective-shear breaking, referred to as forward Kelvin–Helmholtz breaking. The breaking types were parameterized by a scaled wave amplitude a_∞/h_r and a scaled wavenumber $k_\infty\delta$, and an empirical condition based on these two parameters was used to determine a breaking transition criterion for the range of parameters in this study.

For waves at the threshold of instability, the minimum local gradient Richardson number was $0.2 < Ri_g < 0.4$, thus the canonical criterion of $Ri_g \leqslant 0.25$ did not predict breaking in all cases. For shorter waves ($k_\infty\delta > 0.06$), the initial instability developed at the wave crest, leading to backward overturning. For longer waves ($k_\infty\delta < 0.06$), a mechanism related to separation of flow over the ridge seemed to lead to the initial interfacial instability. This alternate breaking mechanism may be sensitive to the Reynolds number and the ridge slope $h_0/2\sigma$.

Even under these idealized laboratory conditions, measuring Ri_g is very difficult. A simplified model is developed to estimate the Richardson number using only scales of the incident wave (a_∞, k_∞), background stratification and topography (δ, h_2, h_1, h_r). Despite the limitations of a constant Ri_g breaking criterion, this rough estimate of Ri_g provides an indication of where in the parameter space interfacial shear is likely to be important. The model also indicates that the empirical shoaling criterion from §4.1 is roughly equivalent to a curve of constant Ri_g for the ridge cases, which is consistent with the idea that both interfacial shear and shoaling processes may contribute to wave breaking. For deeper or more shallow waves relative to the topography, either

shear or nonlinear wave steepening may dominate the breaking process. The model could be applied to a particular case to estimate if an incident wave is likely to break and which processes may be important. However, even if the model can accurately predict that the minimum Richardson number for a given flow is, say, $Ri_g = 0.2$, this is not sufficient to determine whether or not the wave will break, due to the effects of unsteadiness and wave nonlinearity.

It is important to note that the canonical Richardson number criterion of $Ri_g = 0.25$ is not, on its own, sufficient for determining when instability will occur in interfacial wave flows. For increasingly nonlinear waves, the assumptions of this criterion of steady, parallel and uniform flow become less and less appropriate, and the stability boundaries of the flow may be affected. For example, oscillatory shear can have a stabilizing or destabilizing effect on near-critical baroclinic flows (Pedlosky & Thomson 2003). The results of Fringer & Street (2003), Troy & Koseff (2005b) and Fructus *et al.* (2009) indicate that unsteadiness can alter stability boundaries from the canonical values. Incident waves in this study are generated under the same conditions as Troy & Koseff; the only difference is that the waves in this study steepen at a ridge instead of at a contraction in the tank width. The wave frequency, and thus the time scale associated with the wave unsteadiness, should be quite similar between these two studies for a wave of the same incident ka and kd, and one might expect that unsteadiness would lead to a similar critical Ri_g for both cases. But when $Ri_g = 0.2$, the ridge case waves are near breaking or breaking, whereas in the contraction case the waves are stable. This suggests that although unsteadiness tends to decrease the critical Richardson number, the bathymetric interaction can increase the critical value due to nonlinear steepening and flow separation. The combined effect of unsteadiness and bathymetric interactions leads to a critical value of $Ri_g = 0.3 \pm 0.1$, in this study. The exact critical value will likely vary depending on the particular bathymetric interaction. The gradient Richardson number may provide a rough estimate of when interfacial waves may break, but because of the sensitivity of wave stability to unsteadiness and nonlinearity, caution should be taken when applying a constant Ri_g breaking criterion to an internal wave flow.

It is difficult to distinguish whether interfacial shear or wave steepness is the primary cause of the initial wave instability because many waves in this study have both low Ri_g and high nonlinearity (a/h_r). Breaking at a relatively constant Ri_g (Fringer & Street 2003) as well as qualitative features (e.g. figure 2a) suggest that shear plays an important role in the initial wave instability. As the incident wave amplitude is increased, however, qualitative observations show elements of convective instability as well as shear instability (see figure 3), suggesting that both wave steepness and interfacial shear play a role in wave breaking. Because of the complex mixed nature of the wave instability, assuming the wave breaking is either shear or convective in nature does not seem appropriate. Rather than assuming a mixing efficiency based on the instability mechanism, further study is needed to directly measure the mixing efficiency of such breaking events.

REFERENCES

AI, J., LAW, A. W. K. & YU, S. C. M. 2006 On Boussinesq and non-Boussinesq starting forced plumes. *J. Fluid Mech.* **558**, 357–386.

BOEGMAN, L. & IVEY, G. N. 2009 Flow separation and resuspension beneath shoaling nonlinear internal waves. *J. Geophys. Res.* **114**, C02018.

BOEGMAN, L., IVEY, G. N. & IMBERGER, J. 2005 The degeneration of internal waves in lakes with sloping topography. *Limnol. Oceanogr.* **50** (5), 1620–1637.

BOGUCKI, D., DICKEY, T. & REDEKOPP, L. G. 1997 Sediment resuspension and mixing by resonantly generated internal solitary waves. *J. Phys. Oceanogr.* **27** (7), 1181–1196.

CACCHIONE, D. & WUNSCH, C. 1974 Experimental study of internal waves over a slope. *J. Fluid Mech.* **66**, 223–239.

CARR, M. & DAVIES, P. A. 2006 The motion of an internal solitary wave of depression over a fixed bottom boundary in a shallow, two-layer fluid. *Phys. Fluids* **18**, 016601.

CARR, M., DAVIES, P. A. & SHIVARAM, P. 2008 Experimental evidence of internal solitary wave-induced global instability in shallow water benthic boundary layers. *Phys. Fluids* **20** (6), 066603–066603.

CHEN, C. Y., HSU, J. R. C., CHENG, M. H. & CHEN, C. W. 2008 Experiments on mixing and dissipation in internal solitary waves over two triangular obstacles. *Environ. Fluid Mech.* **8** (3), 199–214.

CRIMALDI, J. P. 2008 Planar laser induced fluorescence in aqueous flows. *Exp. Fluids* **44** (6), 851–863.

CRIMALDI, J. P. & KOSEFF, J. R. 2001 High-resolution measurements of the spatial and temporal scalar structure of a turbulent plume. *Exp. Fluids* **31** (1), 90–102.

DALZIEL, S. B., CARR, M., SVEEN, J. K. & DAVIES, P. A. 2007 Simultaneous synthetic schlieren and PIV measurements for internal solitary waves. *Meas. Sci. Technol.* **18** (3), 533–547.

DAVIERO, G. J., ROBERTS, P. J. W. & MAILE, K. 2001 Refractive index matching in large-scale stratified experiments. *Exp. Fluids* **31** (2), 119–126.

DEAN, R. G. & DALRYMPLE, R. A. 1984 Water wave mechanics for engineers and scientists. In *River Edge*. World Scientific. Advanced Series on Ocean Engineering, Vol. 2, 335.

DE SILVA, I. P. D., FERNANDO, H. J. S., EATON, F. & HEBERT, D. 1996 Evolution of Kelvin–Helmholtz billows in nature and laboratory. *Earth Planet. Sci. Lett.* **143** (1), 217–231.

DIAMESSIS, P. J. & REDEKOPP, L. G. 2006 Numerical investigation of solitary internal wave-induced global instability in shallow water benthic boundary layers. *J. Phys. Oceanogr.* **36** (5), 784–812.

DIEZ, F. J., BERNAL, L. P. & FAETH, G. M. 2005 PLIF and PIV measurements of the self-preserving structure of steady round buoyant turbulent plumes in crossflow. *Intl J. Heat Fluid Flow* **26** (6), 873–882.

EMERY, K. O. & GUNNERSON, C. G. 1973 Internal swash and surf. *Proc. Natl Acad. Sci. USA* **70** (8), 2379–2380.

FRINGER, O. B. & STREET, R. L. 2003 The dynamics of breaking progressive interfacial waves. *J. Fluid Mech.* **494**, 319–353.

FRUCTUS, D., CARR, M., GRUE, J., JENSEN, A. & DAVIES, P. A. 2009 Shear induced breaking of large internal waves. *J. Fluid Mech.* **620**, 1–29.

GRUE, J., JENSEN, A., RUSAS, P. & SVEEN, J. K. 2000 Breaking and broadening of internal solitary waves. *J. Fluid Mech.* **413**, 181.

HAZEL, P. 1972 Numerical studies of the stability of inviscid stratified shear flows. *J. Fluid Mech.* **51**, 39–61.

HELFRICH, K. R. 1992 Internal solitary wave breaking and run-up on a uniform slope. *J. Fluid Mech.* **243**, 133–154.

HELFRICH, K. R. & MELVILLE, W. K. 1986 On long nonlinear internal waves over slope-shelf topography. *J. Fluid Mech.* **167**, 285–308.

HELFRICH, K. R. & MELVILLE, W. K. 2006 Long nonlinear internal waves. *Annu. Rev. Fluid Mech.* **38**, 395–425.

HOLYER, J. Y. 1979 Large amplitude progressive interfacial waves. *J. Fluid Mech.* **93**, 433–448.

HOWARD, L. N. 1961 Note on a paper of John W. Miles. *J. Fluid Mech.* **10**, 509–512.

HULT, E. L., TROY, C. D. & KOSEFF, J. R. 2006 Laboratory images of breaking internal waves. *Phys. Fluids* **18**, 091107.

Ivey, G. N. & Nokes, R. I. 1989 Vertical mixing due to the breaking of critical internal waves on sloping boundaries. *J. Fluid Mech.* **204**, 479–500.

Ivey, G. N., Winters, K. B. & De Silva, I. P. D. 2000 Turbulent mixing in a sloping benthic boundary layer energized by internal waves. *J. Fluid Mech.* **418**, 59–76.

Kao, T. W., Pan, F. S. & Renouard, D. 1985 Internal solitons on the pycnocline: generation, propagation, and shoaling and breaking over a slope. *J. Fluid Mech.* **159**, 19–53.

Kunze, E. & Sanford, T. B. 1996 Abyssal mixing: where it is not. *J. Phys. Oceanogr.* **26** (10), 2286–2296.

Law, A. W. K., Wang, H. & Herlina 2003 Combined particle image velocimetry/planar laser induced fluorescence for integral modelling of buoyant jets. *J. Engng Mech.* **129** (10), 1189–1196.

Ledwell, J. R., Montgomery, E. T., Polzin, K. L., St. Laurent, L. C., Schmitt, R. W. & Toole, J. M. 2000 Evidence for enhanced mixing over rough topography in the abyssal ocean. *Nature* **403** (6766), 179–182.

Linden, P. F. & Redondo, J. M. 1991 Molecular mixing in Rayleigh–Taylor instability. Part I. Global mixing. *Phys. Fluids* **3** (5), 1269–1277.

Lueck, R. G. & Mudge, T. D. 1997 Topographically induced mixing around a shallow seamount. *Science* **276**, 1831–1833.

Michallet, H. & Ivey, G. N. 1999 Experiments on mixing due to internal solitary waves breaking on uniform slopes. *J. Geophys. Res.* **104** (C6), 13467–13478.

Miles, J. W. 1961 On the stability of heterogeneous shear flows. *J. Fluid Mech.* **10**, 496–508.

Moum, J. N., Farmer, D. M., Smyth, W. D., Armi, L. & Vagle, S. 2003 Structure and generation of turbulence at interfaces strained by internal solitary waves propagating shoreward over the continental shelf. *J. Phys. Oceanogr.* **33** (10), 2093–2112.

Nagashima, H. 1971 Reflection and breaking of internal waves on a sloping beach. *J. Oceanogr.* **27** (1), 1–6.

Orlanski, I. & Bryan, K. 1969 Formation of the thermocline step structure by large-amplitude internal gravity waves. *J. Geophys. Res.* **74** (28), 6975–6983.

Pawlak, G. & Armi, L. 2000 Vortex dynamics in a spatially accelerating shear layer. *J. Fluid Mech.* **376**, 1–35.

Pedlosky, J. & Thomson, J. 2003 Baroclinic instability of time-dependent currents. *J. Fluid Mech.* **490**, 189–215.

Peltier, W. R. & Caulfield, C. P. 2003 Mixing efficiency in stratified shear flows. *Ann. Rev. Fluid Mech.* **35** (1), 135–167.

Phillips, O. M. 1966 *The Dynamics of the Upper Ocean*. Cambridge University Press.

Polzin, K. L., Toole, J. M., Ledwell, J. R. & Schmitt, R. W. 1997 Spatial variability of turbulent mixing in the abyssal ocean. *Science* **276** (5309), 93–96.

Rehmann, C. R. 1995 Effects of stratification and molecular diffusivity on the mixing efficiency of decaying grid turbulence. PhD thesis, Stanford University, Stanford.

Shavit, U., Lowe, R. L. & Steinbuck, J. V. 2007 Intensity capping: a simple method to improve cross-correlation PIV results. *Exp. Fluids* **42** (2), 225–240.

Sveen, J. K., Guo, Y., Davies, P. A. & Grue, J. 2002 On the breaking of internal solitary waves at a ridge. *J. Fluid Mech.* **469**, 161–188.

Taylor, J. R. 1993 Turbulence and mixing in the boundary layer generated by shoaling internal waves. *Dyn. Atmos. Oceans* **19**, 233–258.

Thorpe, S. A. 1978 On the shape and breaking of finite amplitude internal gravity waves in a shear flow. *J. Fluid Mech.* **85**, 7–31.

Thorpe, S. A. 1987 On the reflection of a train of finite-amplitude internal waves from a uniform slope. *J. Fluid Mech.* **178**, 279–302.

Thorpe, S. A. 1998 Some dynamical effects of internal waves and the sloping sides of lakes. *Phys. Processes Lakes Oceans, Coast. Estuar. Stud.* **54**, 441–460.

Toole, J. M., Schmitt, R. W., Polzin, K. L. & Kunze, E. 1997 Near-boundary mixing above the flanks of a midlatitude seamount. *J. Geophys. Res.* **102**, 947–959.

Troy, C. D. & Koseff, J. R. 2005a The generation and quantitative visualization of breaking internal waves. *Exp. Fluids* **38** (5), 549–562.

Troy, C. D. & Koseff, J. R. 2005b The instability and breaking of long internal waves. *J. Fluid Mech.* **543**, 107–136.

VARIANO, E. A. & COWEN, E. A. 2007 Quantitative imaging of CO2 transfer at an unsheared free surface. In *Transport at the Air-Sea Interface* (ed. C. S. Garbe, R. A. Handler & B. Jähne), pp. 43–57. Springer.

VENAYAGAMOORTHY, S. K. & FRINGER, O. B. 2006 Numerical simulations of the interaction of internal waves with a shelf break. *Phys. Fluids* **18** (7), 76603–76603.

VLASENKO, V. & HUTTER, K. 2002 Numerical experiments on the breaking of solitary internal waves over a slope-shelf topography. *J. Phys. Oceanogr.* **32** (6), 1779–1793.

WALLACE, B. C. & WILKINSON, D. L. 1988 Run-up of internal waves on a gentle slope in a two-layered system. *J. Fluid Mech.* **191**, 419–442.

WESSELS, F. & HUTTER, K. 1996 Interaction of internal waves with a topographic sill in a two-layered fluid. *J. Phys. Oceanogr.* **26** (1), 5–20.

WESTERWEEL, J. & SCARANO, F. 2005 Universal outlier detection for PIV data. *Exp. Fluids* **39** (6), 1096–1100.

ZHU, D. Z. & LAWRENCE, G. A. 2001 Holmboe's instability in exchange flows. *J. Fluid Mech.* **429**, 391–409.